Author(s): Y. Cai and C. Mias
Article Title: Faster 3D finite element time domain – Floquet absorbing
boundary condition modelling using recursive convolution and vector
fitting
Year of publication: 2009
Link to published article:
http://dx.doi.org/10.1049/iet-map:20080029
Publisher statement: © 2009 The Institution of Engineering and
Technology.

Faster 3D FETD ?Floquet ABC Modelling using Recursive Convolution and Vector Fitting

Faster 3D FETD – Floquet ABC Modelling using Recursive Convolution and Vector Fitting

Y. Cai and C. Mias

Abstract: A recursive convolution (RC) based on the vector fitting (VF) method and triangular temporal basis functions is employed to compute the Floquet absorbing boundary condition (FABC) formulation in the vector 3D finite element time domain (FETD) modelling of doubly periodic structures. This novel implementation (VF-RC-FETD-FABC) results in significantly lower computation time requirements than the standard convolution (SC) implementation. The numerical examples presented show reduction in computation time requirements by a factor of at least 3.5. In addition, a time window in excess of 50,000 time-steps is recorded over which practically stable results are obtained. This temporal window is sufficiently large to allow the modelling of many practical problems. Results from four such problems are presented confirming the accuracy and speed of the VF-RC-FETD-FABC software.

1 Introduction

Recently, a finite element time domain (FETD) formulation was proposed to model plane wave scattering from 3D infinite doubly periodic structures [1]. The formulation was based on the accurate Floquet absorbing boundary condition (ABC) which was shown [1] to be superior in versatility and accuracy than the simple ABC [2]. The computation of the Floquet ABC formulation in [1] is, however, time consuming as the convolution integrals present in the formulation are computed in a standard fashion henceforth called the standard convolution (SC). In this paper we show how this time consuming computation can be significantly improved using recursive convolution (RC) [3]. We present numerical results that demonstrate a reduction of computation time by at least a factor of 3.5.

Our research has shown that if the multi-section (4-section) RC (MS-RC) with trapezoidal integration, proposed in the scalar 2D simulations of [4], is employed in the vector 3D FETD-FABC simulations it leads to an early onset of instability. Hence, we propose a more accurate single-section RC implementation based on the vector fitting (VF) method [5] and triangular temporal basis functions [6]. Using this new RC methodology we demonstrate numerically that time windows of practical stability in excess of 50,000 time steps can be achieved.

Such temporal windows enable us to employ the proposed VF-RC-FETD-FABC method to simulate many practical doubly periodic problems.

In section II we present a detailed description of our finite element formulation as our time domain boundary integral formulation and the convolution implementation are significantly different from those of [1]. This difference is mainly due to the final form of our frequency domain boundary integral formulation (see eq.(73)) prior to applying the inverse Laplace transform (ILT). This form is necessary in order to readily implement the RC methodology. We also employ the reciprocal weighting function approach proposed in [7,8] which does not lead to the stability problem associated with eq.(16) of [1]. Section III considers the RC implementation. In section IV numerical results are presented demonstrating the accuracy, speed and stability for practical time windows of the developed VF-RC-FETD-FABC code. Section V concludes the paper.

2   Formulation

2.1   Floquet harmonic expansion

Referring to Fig.1, the propagation vector, $\textbf{\textit{k}}_0$, of the incident wave is determined by the elevation angle, θ^{inc}, and the azimuth angle, ϕ^{inc}. The direction of the electric field vector, $\textbf{E}^{inc}$, is determined by $\textbf{\textit{k}}_0$ and the polarisation angle η^{inc}. The incident electric field can be expressed in the frequency domain, where the assumed $\exp(j\omega t)$ time variation is suppressed, as

$$\textbf{E}^{inc}(\textbf{r}) = \left(\textbf{I}_{t,00} + I_{z,00}\hat{\textbf{z}}\right)e^{-j\textbf{k}_0\bullet\textbf{r}} = I_0 \begin{bmatrix} \left(\sin\eta^{inc}\cos\theta^{inc}\cos\phi^{inc} - \cos\eta^{inc}\sin\phi^{inc}\right)\hat{\textbf{x}} \\ + \left(\sin\eta^{inc}\cos\theta^{inc}\sin\phi^{inc} + \cos\eta^{inc}\cos\phi^{inc}\right)\hat{\textbf{y}} \\ - \sin\eta^{inc}\sin\theta^{inc}\;\hat{\textbf{z}} \end{bmatrix}e^{-j\textbf{k}_0\bullet\textbf{r}} \qquad (1)$$

In (1), $\textbf{r} = x\hat{\textbf{x}} + y\hat{\textbf{y}} + z\hat{\textbf{z}}$ and I_0 is the amplitude of the incident field. Tangential and normal components to the non-periodic surfaces S_1 and S_2 (see Fig.1) are indicated by the subscripts 't' and 'z' respectively. S_1 is located at $z = z_1$. S_2 is located at $z = z_2$.

From Floquet's theorem [9], the field within the unit cell of the infinite planar doubly periodic structure (Fig. 1) illuminated by the aforementioned plane wave can be expressed as

$$\textbf{E}(\textbf{r}) = \textbf{E}_p(\textbf{r})e^{-jk_0\boldsymbol{\tau}\bullet\textbf{r}} \qquad (2)$$

where $\textbf{E}_p$ is the periodic part of the electric field. $k_0 = |\textbf{k}_0| = \omega/c$ is the wavenumber in free space and c is the speed of light in free space. The tangential vector $\boldsymbol{\tau}$ is defined as

$$\boldsymbol{\tau} = \tau_x \hat{\mathbf{x}} + \tau_y \hat{\mathbf{y}} = \sin\theta^{inc}\cos\phi^{inc}\,\hat{\mathbf{x}} + \sin\theta^{inc}\sin\phi^{inc}\,\hat{\mathbf{y}} \tag{3}$$

Along the periodic boundary pairs PB_x and PB_y (see Fig.1) $\mathbf{E}_p$ satisfies the periodic boundary conditions:

PB_x:
$$\mathbf{E}_p\left(x + D_x, y, z\right) = \mathbf{E}_p\left(x, y, z\right) \tag{4}$$

PB_y:
$$\mathbf{E}_p\left(x, y + D_y, z\right) = \mathbf{E}_p\left(x, y, z\right) \tag{5}$$

where D_x and D_y are the periods along the x and y directions respectively. Using Fourier series, the periodic part of the reflected and transmitted scattered fields $\mathbf{E}_p^{ref}$ and $\mathbf{E}_p^{tran}$ at S_1 and S_2 respectively are expanded as an infinite summation of Floquet harmonics

$$\mathbf{E}_p^{ref}\left(x, y, z_1\right) = \sum_{m=-\infty}^{\infty}\sum_{n=-\infty}^{\infty}\left(\mathbf{R}_{t,mn} + R_{z,mn}\hat{\mathbf{z}}\right)e^{-j\boldsymbol{\rho}_{t,mn}\bullet\mathbf{r}}e^{+jk_{z,mn}z_1} \tag{6}$$

$$\mathbf{E}_p^{tran}\left(x, y, z_2\right) = \sum_{m=-\infty}^{\infty}\sum_{n=-\infty}^{\infty}\left(\mathbf{T}_{t,mn} + T_{z,mn}\hat{\mathbf{z}}\right)e^{-j\boldsymbol{\rho}_{t,mn}\bullet\mathbf{r}}e^{-jk_{z,mn}z_2} \tag{7}$$

where $\mathbf{R}_{t,mn} + R_{z,mn}\hat{\mathbf{z}}$ and $\mathbf{T}_{t,mn} + T_{z,mn}\hat{\mathbf{z}}$ are the vector amplitudes of the reflected and transmitted (m,n)th Floquet harmonics. The tangential vector $\boldsymbol{\rho}_{t,mn}$ is defined as

$$\boldsymbol{\rho}_{t,mn} = \rho_{x,m}\hat{\mathbf{x}} + \rho_{y,n}\hat{\mathbf{y}} = \frac{2\pi m}{D_x}\hat{\mathbf{x}} + \frac{2\pi n}{D_y}\hat{\mathbf{y}} \tag{8}$$

For the (m,n)th propagating or evanescent Floquet harmonic

$$k_{z,mn} = \begin{cases} \sqrt{k_0^2 - \left|\mathbf{k}_{t,mn}\right|^2} & k_0^2 \geq \left|\mathbf{k}_{t,mn}\right|^2 \quad propagating \\ -j\sqrt{\left|\mathbf{k}_{t,mn}\right|^2 - k_0^2} & k_0^2 < \left|\mathbf{k}_{t,mn}\right|^2 \quad evanescent \end{cases} \tag{9}$$

and

$$\mathbf{k}_{t,mn} = \left(k_0\tau_x + \rho_{x,m}\right)\hat{\mathbf{x}} + \left(k_0\tau_y + \rho_{y,n}\right)\hat{\mathbf{y}} \tag{10}$$

The periodic part of the incident field is defined at S_1 as

$$\mathbf{E}_p^{inc}\left(x, y, z_1\right) = \left(\mathbf{I}_{t,00} + I_{z,00}\hat{\mathbf{z}}\right)e^{-jk_{z,00}z_1} \tag{11}$$

Starting from Gauss' Law in free space ($\nabla\bullet\varepsilon_0\mathbf{E} = 0$), the following equation is valid for each (m,n)th Floquet harmonic [8]

$$X_{z,mn} = \mp\frac{\mathbf{k}_{t,mn}\bullet\mathbf{X}_{t,mn}}{k_{z,mn}} \tag{12}$$

where X is R, T or I. The $-/+$ sign denotes propagation in the $+/-$ z-direction respectively.

Using orthogonality relations, over the non-periodic boundary surfaces S_1 and S_2, the tangential components of the vector amplitudes of the reflected (m,n)th Floquet harmonic and the transmitted (m,n)th Floquet harmonic can be obtained

$$\mathbf{R}_{t,mn} = \frac{1}{\alpha}\int_{S_1}\mathbf{E}_{p,t}\left(z_1\right)e^{+j\boldsymbol{\rho}_{t,mn}\bullet\mathbf{r}}e^{-jk_{z,mn}z_1}dS - \delta_{mn,00}\mathbf{I}_{t,00}\,e^{-2jk_{z,00}z_1} \tag{13}$$

$$\mathbf{T}_{t,mn} = \frac{1}{\alpha}\int_{S_2}\mathbf{E}_{p,t}\left(z_2\right)e^{+j\boldsymbol{\rho}_{t,mn}\bullet\mathbf{r}}e^{+jk_{z,mn}z_2}dS \tag{14}$$

where $\alpha = D_x D_y$. The $\mathbf{E}_{p,t}(z_1)$ and $\mathbf{E}_{p,t}(z_2)$ are the tangential components of the periodic part of the total field on S_1 and S_2. The Kronecker delta function is given as

$$\delta_{mn,00} = \begin{cases} 1 & (m,n)=(0,0) \\ 0 & (m,n)\neq(0,0) \end{cases} \tag{15}$$

2.2   Finite Element Frequency Domain formulation

The Galerkin weighted residual method is employed to solve the vector wave equation [8]. The weighted residual is integrated over the computation domain and the divergence theorem is applied to obtain

$$\int_V \frac{1}{\mu_r}\left[(\nabla\times\mathbf{W})\bullet(\nabla\times\mathbf{E})\right]dV - k_0^2\int_V \varepsilon_r(\mathbf{W}\bullet\mathbf{E})dV = \oint_s \mathbf{W}\bullet\left[\frac{1}{\mu_r}(\nabla\times\mathbf{E})\times\hat{\mathbf{n}}\right]dS \tag{16}$$

where μ_r and ε_r are the relative permeability and relative permittivity respectively. $\hat{\mathbf{n}}$ is the normal vector to the unit cell surface S and points outwards. For simplicity, it is assumed that the computation domain is lossless and source free.

In (16), $\mathbf{W}$ is the reciprocal weighting function [7, 8],

$$\mathbf{W}(\mathbf{r}) = \mathbf{W}_p(\mathbf{r})e^{+jk_0\boldsymbol{\tau}\bullet\mathbf{r}} \tag{17}$$

where $\mathbf{W}_p(\mathbf{r})$ satisfies the periodic boundary conditions (4,5)

$$PB_x: \qquad \mathbf{W}_p\left(x + D_x, y, z\right) = \mathbf{W}_p\left(x, y, z\right) \tag{18}$$

$$PB_y: \qquad \mathbf{W}_p\left(x, y + D_y, z\right) = \mathbf{W}_p\left(x, y, z\right) \tag{19}$$

By making use of (2) and (17), we obtain

$$\nabla\times\mathbf{E} = e^{-jk_0\boldsymbol{\tau}\bullet\mathbf{r}}\left[(\nabla\times\mathbf{E}_p) - jk_0(\boldsymbol{\tau}\times\mathbf{E}_p)\right] \tag{20}$$

$$\nabla\times\mathbf{W} = e^{+jk_0\boldsymbol{\tau}\bullet\mathbf{r}}\left[(\nabla\times\mathbf{W}_p) + jk_0(\boldsymbol{\tau}\times\mathbf{W}_p)\right] \tag{21}$$

$$W \bullet E = W_p \bullet E_p \tag{22}$$

Eqs.(20-22) are substituted into (16) in order to re-write (16) in terms of E_p and W_p as follows

$$\int_V \frac{1}{\mu_r} \left[(\nabla \times W_p) \bullet (\nabla \times E_p) \right] dV - k_0^2 \int_V \left(\varepsilon_r - \frac{\sin^2 \theta^{inc}}{\mu_r} \right) (W_p \bullet E_p) dV - k_0^2 \int_V \frac{1}{\mu_r} (\tau \bullet W_p)(\tau \bullet E_p) dV$$

$$+ jk_0 \int_V \frac{1}{\mu_r} \left[(\tau \times W_p) \bullet (\nabla \times E_p) - (\tau \times E_p) \bullet (\nabla \times W_p) \right] dV = \underbrace{\oint_S W_p \bullet \left\{ \frac{1}{\mu_r} \left[(\nabla \times E_p) - jk_0 (\tau \times E_p) \right] \times \hat{n} \right\} dS}_{U^S(\omega)}$$

$$\tag{23}$$

The periodic part of the field, E_p, is chosen as the working variable. The time-domain justification for doing so is given in [10] where the Finite Difference Time Domain method was applied to the modelling of periodic structures. For each periodic boundary pair, the normal unit vectors $\hat{n}$ of the boundaries have opposite directions. Because of this fact and the boundary conditions, eqs. (4, 5, 18, 19), the surface integral terms in (23) along the periodic boundaries cancel out each other. Hence the surface integral term $U^S(\omega)$ is reduced to

$$U^S(\omega) = \int_{S_{1,2}} W_p \bullet \left\{ \frac{1}{\mu_r} \left[(\nabla \times E_p) - jk_0 (\tau \times E_p) \right] \times \hat{n} \right\} dS = \int_{S_{1,2}} \frac{1}{\mu_r} W_{p,t} \bullet \left[\frac{\partial E_{p,t}}{\partial n} - \left(\nabla_t E_{p,n} - jk_0 \tau E_{p,n} \right) \right] dS$$

$$\tag{24}$$

where $W_{p,t} = W_{p,x} \hat{x} + W_{p,y} \hat{y}$, $E_{p,n}$ is the normal component of the periodic part of the total field on S_1 or S_2. $\nabla_t = \partial/\partial x \hat{x} + \partial/\partial y \hat{y}$ denotes the tangential gradient operator. Using (6, 7, 13, 14), the normal derivative terms of $E_{p,t}$ in (24) are expressed as

$$\left. \frac{\partial E_{p,t}}{\partial z} \right|_{S_1} = \left(-2\gamma_{z,00} \right) I_{t,00} e^{-\gamma_{z,00} z_1} + \frac{1}{\alpha} \sum_{m=-\infty}^{\infty} \sum_{n=-\infty}^{\infty} \gamma_{z,mn} \left[\int_{S_1} E_{p,t}(z_1) e^{j\rho_{t,mn} \bullet r'} dS' \right] e^{-j\rho_{t,mn} \bullet r} \tag{25}$$

$$\left. \frac{\partial E_{p,t}}{\partial z} \right|_{S_2} = -\frac{1}{\alpha} \sum_{m=-\infty}^{\infty} \sum_{n=-\infty}^{\infty} \gamma_{z,mn} \left[\int_{S_2} E_{p,t}(z_2) e^{j\rho_{t,mn} \bullet r'} dS' \right] e^{-j\rho_{t,mn} \bullet r} \tag{26}$$

where $\gamma_{z,mn} = jk_{z,mn}$.

Using (12), the following relation is derived

$$\nabla_t X_{z,mn} - jk_0 \tau X_{z,mn} = \mp \frac{k_{t,mn}}{\gamma_{z,mn}} \left(k_{t,mn} \bullet X_{t,mn} \right) \tag{27}$$

By making use of (6, 7, 13, 14) and (27) the second term in the square brackets in (24) can be re-written as

$$\left(\nabla_t E_{p,z} - jk_0\tau E_{p,z}\right)\Big|_{S_1} = -\frac{2\mathbf{k}_{t,00}}{\gamma_{z,00}}\left(\mathbf{k}_{t,00}\bullet\mathbf{I}_{t,00}\,e^{-\gamma_{z,00}z_1}\right)$$

$$+\frac{1}{\alpha}\sum_{n=-\infty}^{+\infty}\sum_{m=-\infty}^{+\infty}\frac{\mathbf{k}_{t,mn}}{\gamma_{z,mn}}\left\{\mathbf{k}_{t,mn}\bullet\left[\int_{S_1}\mathbf{E}_{p,t}\left(z_1\right)e^{j\boldsymbol{\rho}_{t,mn}\bullet\mathbf{r}'}dS'\right]e^{-j\boldsymbol{\rho}_{t,mn}\bullet\mathbf{r}}\right\}$$

(28)

$$\left(\nabla_t E_{p,z} - jk_0\tau E_{p,z}\right)\Big|_{S_2} = -\frac{1}{\alpha}\sum_{n=-\infty}^{+\infty}\sum_{m=-\infty}^{+\infty}\frac{\mathbf{k}_{t,mn}}{\gamma_{z,mn}}\left\{\mathbf{k}_{t,mn}\bullet\left[\int_{S_2}\mathbf{E}_{p,t}\left(z_2\right)e^{j\boldsymbol{\rho}_{t,mn}\bullet\mathbf{r}'}dS'\right]e^{-j\boldsymbol{\rho}_{t,mn}\bullet\mathbf{r}}\right\}$$

(29)

Note $E_{p,n} = -E_{p,z}$ on S_1 and $E_{p,n} = E_{p,z}$ on S_2. Eqs. (25, 26, 28, 29) are employed to re-write the surface integral (24) as follows

$$U^S\left(\omega\right) = F^S\left(\omega\right) - \Omega^1\left(\omega\right) - \Omega^2\left(\omega\right)$$

(30)

where

$$F^S\left(\omega\right) = 2\gamma_{z,00}\left(\int_{S_1}\mathbf{W}_{p,t}dS\right)\bullet\left(\mathbf{I}_{t,00}e^{-\gamma_{z,00}z_1}\right) - \frac{2}{\gamma_{z,00}}\left(\mathbf{k}_{t,00}\bullet\int_{S_1}\mathbf{W}_{p,t}dS\right)\left(\mathbf{k}_{t,00}\bullet\mathbf{I}_{t,00}e^{-\gamma_{z,00}z_1}\right)$$

(31)

$\Omega^1(\omega)$ and $\Omega^2(\omega)$ are given by (72) in the Appendix.

2.3   Finite Element Time Domain formulation

By applying the ILT to (23), we obtain

$$\int_V\frac{1}{\mu_r}\left[\left(\nabla\times\mathbf{W}_p\right)\bullet\left(\nabla\times\mathbf{E}_p\right)\right]dV + \frac{1}{c^2}\int_V\left(\varepsilon_r - \frac{\sin^2\theta^{inc}}{\mu_r}\right)\left(\mathbf{W}_p\bullet\frac{\partial^2\mathbf{E}_p}{\partial t^2}\right)dV + \frac{1}{c^2}\int_V\frac{1}{\mu_r}\left(\boldsymbol{\tau}\bullet\mathbf{W}_p\right)\left(\boldsymbol{\tau}\bullet\frac{\partial^2\mathbf{E}_p}{\partial t^2}\right)dV$$

$$+\frac{1}{c}\int_V\frac{1}{\mu_r}\left[\left(\boldsymbol{\tau}\times\mathbf{W}_P\right)\bullet\left(\nabla\times\frac{\partial\mathbf{E}_p}{\partial t}\right) - \left(\nabla\times\mathbf{W}_p\right)\bullet\left(\boldsymbol{\tau}\times\frac{\partial\mathbf{E}_p}{\partial t}\right)\right]dV = F^S\left(t\right) - \Omega^1\left(t\right) - \Omega^2\left(t\right)$$

(32)

where $\mathbf{E}_p$ is now a time dependent variable and

$$F^S\left(t\right) = \frac{2\cos\theta^{inc}}{c}\left(\int_{S_1}\mathbf{W}_{p,t}dS\right)\bullet\frac{d}{dt}\left[\mathbf{I}_{t,00}\left(t - \frac{\cos\theta^{inc}z_1}{c}\right)\right]$$

$$+\frac{2}{\cos\theta^{inc}c}\left(\boldsymbol{\tau}\bullet\int_{S_1}\mathbf{W}_{p,t}dS\right)\left\{\boldsymbol{\tau}\bullet\frac{d}{dt}\left[\mathbf{I}_{t,00}\left(t - \frac{\cos\theta^{inc}z_1}{c}\right)\right]\right\}$$

(33)

The time-domain terms $\Omega^1(t)$ and $\Omega^2(t)$ are given by (81) in the Appendix where their derivation is also shown.

The computation domain is discretised using 6 degree of freedom (d.o.f.) tetrahedral and 3 d.o.f. triangular edge elements [11]. The field within an edge element e is interpolated as

$$\mathbf{E}_p(\mathbf{r};t) = \sum_{j=1}^{Q_e} \mathbf{N}_j^e(\mathbf{r}) E_{p,j}(t) \tag{34}$$

where $Q_e = 6$ for a tetrahedral element and $Q_e = 3$ for a triangular element. The vector test (weighting) functions are also chosen from the same set of basis functions [8, 11]

$$\mathbf{W}_p(\mathbf{r}) = \mathbf{N}_i^e(\mathbf{r}), \quad i = 1, \ldots, Q_e \tag{35}$$

Following discretisation of (32) using (34, 35), the following matrix equation is obtained (note that for a periodic boundary pair the boundaries have identical finite element meshes)

$$\left[\mathbf{T}^V\right]\frac{d^2\{E_p(t)\}}{dt^2} + \left[\mathbf{B}^V\right]\frac{d\{E_p(t)\}}{dt} + \left[\mathbf{S}^V\right]\{E_p(t)\} = \{\mathbf{F}^S(t)\} - \{\mathbf{\Omega}^1(t)\} - \{\mathbf{\Omega}^2(t)\} \tag{36}$$

where the superscript V indicates the volume region matrices. [ ] and { } denote a matrix and column vector respectively. $[\mathbf{T}^V]$, $[\mathbf{B}^V]$ and $[\mathbf{S}^V]$ are given in [2, eqs.(21, 22, 24)]. Here, we focus on the discretisation of the surface integral formulation at the right-hand side of (36) which is different from [1]. Along the non-periodic boundaries S_1 and S_2 the test and basis functions are expressed as follows

$$\mathbf{N}_i^k(x,y) = N_{x,i}^k(x,y)\hat{\mathbf{x}} + N_{y,i}^k(x,y)\hat{\mathbf{y}} \tag{37}$$

$$\mathbf{N}_j^l(x,y) = N_{x,j}^l(x,y)\hat{\mathbf{x}} + N_{y,j}^l(x,y)\hat{\mathbf{y}} \tag{38}$$

where the subscripts i and j and superscripts k and l denote the ith edge in the kth element and jth edge in the lth element respectively. Using (37, 38), the entries of the column vectors $\{\mathbf{F}^S(t)\}$ and $\{\mathbf{\Omega}^g(t)\}$ in eq.(36) are obtained as

$$\begin{aligned}
F_i^S &= \frac{2\cos\theta^{inc}}{c}\left(\int_{S_k}\mathbf{N}_i^k dS\right)\bullet\frac{d}{dt}\left[\mathbf{I}_{t,00,i}\left(t - \frac{\cos\theta^{inc} z_1}{c}\right)\right] \\
&+ \frac{2}{\cos\theta^{inc} c}\left(\boldsymbol{\tau}\bullet\int_{S_k}\mathbf{N}_i^k dS\right)\left\{\boldsymbol{\tau}\bullet\frac{d}{dt}\left[\mathbf{I}_{t,00,i}\left(t - \frac{\cos\theta^{inc} z_1}{c}\right)\right]\right\}
\end{aligned} \tag{39}$$

$$\begin{aligned}
\Omega_i^g(t) &= \sum_{j=1}^{3}\left\{\sum_{m=-\infty}^{\infty}\sum_{n=-\infty}^{\infty}\sum_{q=1}^{4}\left[\Gamma_{ij,mn}^{(q)}\xi_{mn}^{(q)}(t)\right]\right\} * E_{p,j}(t) \\
&\approx \sum_{j=1}^{3}\left\{\sum_{m=-M_F}^{M_F}\sum_{n=-N_F}^{N_F}\sum_{q=1}^{4}\left[\Gamma_{ij,mn}^{(q)}\xi_{mn}^{(q)}(t)\right]\right\} * E_{p,j}(t)
\end{aligned} \tag{40}$$

where the symbol '*' denotes the convolution operator. Note that in the computations a finite number of Floquet

harmonics is considered ($-M_F \leq m \leq M_F$ and $-N_F \leq n \leq N_F$).

In (40), the time independent terms $\Gamma_{ij,mn}^{(q)}$ are given as

$$\Gamma_{ij,mn}^{(1)} = \int_{S_k} N_{x,i}^k \, e^{-j\boldsymbol{\rho}_{t,mn}\bullet\mathbf{r}} dS \int_{S_l} N_{x,j}^l e^{+j\boldsymbol{\rho}_{t,mn}\bullet\mathbf{r}} dS$$
$$+ \int_{S_k} N_{y,i}^k \, e^{-j\boldsymbol{\rho}_{t,mn}\bullet\mathbf{r}} dS \int_{S_l} N_{y,j}^l e^{+j\boldsymbol{\rho}_{t,mn}\bullet\mathbf{r}} dS \tag{41}$$

$$\Gamma_{ij,mn}^{(2)} = \int_{S_k} N_{x,i}^k \, e^{-j\boldsymbol{\rho}_{t,mn}\bullet\mathbf{r}} dS \int_{S_l} N_{x,j}^l e^{+j\boldsymbol{\rho}_{t,mn}\bullet\mathbf{r}} dS \tag{42}$$

$$\Gamma_{ij,mn}^{(3)} = \int_{S_k} N_{y,i}^k \, e^{-j\boldsymbol{\rho}_{t,mn}\bullet\mathbf{r}} dS \int_{S_l} N_{y,j}^l e^{+j\boldsymbol{\rho}_{t,mn}\bullet\mathbf{r}} dS \tag{43}$$

$$\Gamma_{ij,mn}^{(4)} = \int_{S_k} N_{x,i}^k \, e^{-j\boldsymbol{\rho}_{t,mn}\bullet\mathbf{r}} dS \int_{S_l} N_{y,j}^l e^{+j\boldsymbol{\rho}_{t,mn}\bullet\mathbf{r}} dS$$
$$+ \int_{S_k} N_{y,i}^k \, e^{-j\boldsymbol{\rho}_{t,mn}\bullet\mathbf{r}} dS \int_{S_l} N_{x,j}^l e^{+j\boldsymbol{\rho}_{t,mn}\bullet\mathbf{r}} dS \tag{44}$$

The $\xi_{mn}^{(q)}(t)$ functions in (40) are derived in the Appendix,

$$\xi_{mn}^{(q)}(t) = h_{mn}^{(q)}(t) + C_0^{(q)} C_4^{(q)} \delta'(t) + jC_0^{(q)} C_{5,mn}^{(q)} \delta(t) \tag{45}$$

where $\delta(t)$ and $\delta'(t)$ are the Dirac delta function and its first order time derivative respectively.

The terms $\Gamma_{ij,mn}^{(q)}$ and $\xi_{mn}^{(q)}(t)$ have the property

$$\Gamma_{ij,-m-n}^{(q)} = \overline{\Gamma}_{ij,mn}^{(q)} \quad, \quad \xi_{-m-n}^{(q)}(t) = \overline{\xi}_{mn}^{(q)}(t) \tag{46}$$

where $\overline{\Gamma}, \overline{\xi}$ are the complex conjugates of Γ, ξ respectively.

Thus, we have

$$\Gamma_{ij,mn}^{(q)} \xi_{mn}^{(q)}(t) + \Gamma_{ij,-m-n}^{(q)} \xi_{-m-n}^{(q)}(t) = 2\text{Re}\left[\Gamma_{ij,mn}^{(q)} \xi_{mn}^{(q)}(t)\right] \tag{47}$$

where Re[ ] denotes the real part of [ ]. Hence, (40) is re-written as

$$\Omega_i^g(t) = \sum_{j=1}^{3} \left\{ \sum_{q=1}^{4} \left[\Gamma_{ij,00}^{(q)} \xi_{00}^{(q)}(t) \right] \right\} * E_{p,j}(t)$$
$$+ 2\sum_{j=1}^{3} \left\{ \sum_{\substack{n=1 \\ (m=0)}}^{N_F} \sum_{q=1}^{4} \text{Re}\left[\Gamma_{ij,mn}^{(q)} \xi_{mn}^{(q)}(t) \right] \right\} * E_{p,j}(t) \tag{48}$$
$$+ 2\sum_{j=1}^{3} \left\{ \sum_{m=1}^{M_F} \sum_{n=-N_F}^{N_F} \sum_{q=1}^{4} \text{Re}\left[\Gamma_{ij,mn}^{(q)} \xi_{mn}^{(q)}(t) \right] \right\} * E_{p,j}(t)$$

Since

$$\delta(t) * E_{p,j}(t) = E_{p,j}(t) \quad, \quad \delta'(t) * E_{p,j}(t) = \frac{dE_{p,j}(t)}{dt} \tag{49}$$

eq.(48) can be expressed, using (45), as

$$\Omega_i^g(t) = \sum_{j=1}^{3} B_{ij}^S \frac{dE_{p,j}(t)}{dt} + \sum_{j=1}^{3} S_{ij}^S E_{p,j}(t) + \Psi_i^S(t) \tag{50}$$

where the matrix entries B_{ij}^S, S_{ij}^S and Ψ_i^S are given as follows

$$B_{ij}^S = \sum_{q=1}^{4}\left[\Gamma_{ij,00}^{(q)} C_0^{(q)} C_4^{(q)}\right] + 2\sum_{\substack{n=1\\(m=0)}}^{N_F}\sum_{q=1}^{4}\mathrm{Re}\left[\Gamma_{ij,mn}^{(q)} C_0^{(q)} C_4^{(q)}\right] + 2\sum_{m=1}^{M_F}\sum_{n=-N_F}^{N_F}\sum_{q=1}^{4}\mathrm{Re}\left[\Gamma_{ij,mn}^{(q)} C_0^{(q)} C_4^{(q)}\right] \tag{51}$$

$$S_{ij}^S = 2\sum_{\substack{n=1\\(m=0)}}^{N_F}\sum_{q=1}^{4}\mathrm{Re}\left[\Gamma_{ij,mn}^{(q)} j C_0^{(q)} C_{5,mn}^{(q)}\right] + 2\sum_{m=1}^{M_F}\sum_{n=-N_F}^{N_F}\sum_{q=1}^{4}\mathrm{Re}\left[\Gamma_{ij,mn}^{(q)} j C_0^{(q)} C_{5,mn}^{(q)}\right] \tag{52}$$

$$\Psi_i^S(t) = 2\sum_{j=1}^{3}\left\{\sum_{\substack{n=1\\(m=0)}}^{N_F}\sum_{q=1}^{4}\mathrm{Re}\left[\Gamma_{ij,mn}^{(q)} h_{mn}^{(q)}(t)\right]\right\} * E_{p,j}(t) + 2\sum_{j=1}^{3}\left\{\sum_{m=1}^{M_F}\sum_{n=-N_F}^{N_F}\sum_{q=1}^{4}\mathrm{Re}\left[\Gamma_{ij,mn}^{(q)} h_{mn}^{(q)}(t)\right]\right\} * E_{p,j}(t) \tag{53}$$

Using (50), (36) can be re-written as

$$[\mathbf{T}^V]\frac{d^2\{E_p(t)\}}{dt^2} + [\mathbf{B}^V + \mathbf{B}^S]\frac{d\{E_p(t)\}}{dt} + [\mathbf{S}^V + \mathbf{S}^S]\{E_p(t)\} + \{\mathbf{\Psi}^S\} = \{\mathbf{F}^S\} \tag{54}$$

The time functions are discretised with the aid of the Newmark-beta method [12, 13] which employs three time steps: M+1, M and M-1. M+1 is the future step at which the field will be evaluated. As in [4], the Newmark-beta time discretisation is applied to all time functions except $\{\mathbf{F}^S\}$ and the convolution terms in $\{\mathbf{\Psi}^S\}$. The latter are evaluated at $t = M\Delta t$. Thus, the following time discretised matrix equation is obtained

$$\left(\frac{[\mathbf{T}]}{\Delta t^2} + \frac{[\mathbf{B}]}{2\Delta t} + \frac{[\mathbf{S}]}{4}\right)\{E_p\}^{M+1} = \left(\frac{2[\mathbf{T}]}{\Delta t^2} - \frac{[\mathbf{S}]}{2}\right)\{E_p\}^M + \left(-\frac{[\mathbf{T}]}{\Delta t^2} + \frac{[\mathbf{B}]}{2\Delta t} - \frac{[\mathbf{S}]}{4}\right)\{E_p\}^{M-1} - \{\mathbf{\Psi}^S\}^M + \{\mathbf{F}^S\}^M$$

$$\tag{55}$$

where $[\mathbf{T}]=[\mathbf{T}^V]$, $[\mathbf{B}]=[\mathbf{B}^V+\mathbf{B}^S]$ and $[\mathbf{S}]=[\mathbf{S}^V+\mathbf{S}^S]$.

3 VF-RC Formulation

The convolution term $h_{mn}^{(q)}(t) * E_{p,j}(t)$ in (53) is evaluated using a single section RC. The RC has lower computer memory requirements than the SC in [1]. In addition, although the single section RC uses more exponential terms than the multi-section RC (MS-RC) approach described in [4] it maintains the speed advantage of the RC over the SC. Furthermore, as the single-section RC requires the memory storage of two time-step values of the working variable at the non-periodic boundaries, it needs less computer memory than the MS-RC and dispenses with the

need to decide the various section limits and the number of exponential terms per section that was necessary in [4].

The use of a single section RC over a large time window is made possible using the vector fitting (VF) method [5].

As it will be numerically demonstrated in section IV, the accuracy of the VF method coupled with the use of

triangular basis functions results in a 3D RC-FETD method that exhibits practical stability over a longer time

period than the one achieved using the 4-section MS-RC with trapezoidal integration proposed in [4]. Details of

the VF-RC implementation follow.

In our 3D FETD-FABC simulations, there are three time functions (98-100) that need to be expressed by a

summation of exponential functions. For clarity, let $\chi=\omega_{ab}t$. The functions are re-written as

$$f_{1,mn}(\chi)=e^{j(\omega_a/\omega_{ab})\chi}J_0(\chi) \tag{56}$$

$$f_{2,mn}(\chi)=j\omega_{ab}e^{j(\omega_a/\omega_{ab})\chi}J_1(\chi) \tag{57}$$

$$f_{3,mn}(\chi)=\omega_{ab}^2e^{j(\omega_a/\omega_{ab})\chi}J_1(\chi)/\chi \tag{58}$$

To use the VF method, the Bessel function terms must first be transformed in the Laplace domain

$$\mathsf{L}[J_0(\chi)]=1/\sqrt{s^2+1} \tag{59}$$

$$\mathsf{L}[J_1(\chi)]=1/\left[\left(\sqrt{s^2+1}\right)\left(s+\sqrt{s^2+1}\right)\right] \tag{60}$$

$$\mathsf{L}[J_1(\chi)/\chi]=\sqrt{s^2+1}-s \tag{61}$$

The MATLAB software package 'VECTFIT', available in the public domain [14], is then employed to obtain

rational approximations of the Laplace transforms (59-61). For example, the function (59) is approximated as

$$\mathsf{L}[J_0(\chi)]=1/\sqrt{s^2+1}\approx\sum_{i=1}^{Q}\frac{a_i}{s-b_i} \tag{62}$$

where the coefficients (a_i, b_i) are complex numbers and Q denotes the number of exponential terms in the

approximation.

Similar approximations hold for the other functions. For the purpose of repeating the work, some of the

computed coefficients, obtained by VECFIT, are listed in Table-1 along with the input parameters to obtain these

coefficients. Note that the coefficients of each function are generic as they are the same for all harmonics (m, n)

and for all structures. For example, the coefficients of Table-1 were used for all the models in section IV. From

(56) and the ILT of (62), the approximated time-domain function $f_{1,mn}(\chi)$ can be expressed as

$$\tilde{f}_{1,mn}(\chi)=e^{j(\omega_a/\omega_{ab})\chi}\sum_{i=1}^{Q}a_ie^{b_i\chi}=\sum_{i=1}^{Q}A_ie^{B_i\chi} \tag{63}$$

Similar expressions can be obtained for the functions $f_{2,mn}(\chi)$ and $f_{3,mn}(\chi)$. The absolute approximation errors, $e(\chi) = |\tilde{f}(\chi) - f(\chi)|$, of the VF method are, for all functions, smaller than those using the 4-section MS approach of [4]. The lower these errors are the larger is the achieved time window of practical stability.

The discrete form of the VF-RC formulation will now be obtained. Note that the convolution integral is performed for all the d.o.f. associated with the non-periodic boundary surfaces and the time functions $h_{mn}^{(q)}(t)$ associated with each harmonic. However, for simplicity we will consider only one d.o.f , $E_{p,j}(t)$, of the working variable vector $\{E_p(t)\}$ and only the function $\tilde{f}_{1,mn}(\chi)$ of (63). Similar discrete formulations hold true for the other d.o.f. and time functions. Using (63), the single section RC formulation is

$$R^M = \sum_{i=1}^{Q} \mathfrak{R}_i^M = \sum_{i=1}^{Q} \left\{ e^{B_i \omega_{ab} \Delta t} \mathfrak{R}_i^{M-1} \right\} + \sum_{i=1}^{Q} \left\{ \int_{(M-1)\Delta t}^{M\Delta t} \left[A_i e^{B_i \omega_{ab}(M\Delta t - \tau)} \right] E_{p,j}(\tau) d\tau \right\} \tag{64}$$

where R^M is the convolution value at the current Mth time step and $\mathfrak{R}_i$ is the convolution value associated with each exponential term. The formulation is derived in [4].

The evaluation of the integral term in (64) affects the stability of the FETD method [1]. The use of the trapezoidal integration is shown in [4]. Here, we present the evaluation of this term using the more accurate triangular temporal basis functions [6]. Using the triangular temporal basis function, the field variable is interpolated over a single time-step period, $t_{M-1} \le t \le t_M$, as follows

$$E_{p,j}(t) \approx E_{p,j}^{M-1} \left[-\frac{1}{\Delta t}(t - t_M) \right] + E_{p,j}^{M} \left[\frac{1}{\Delta t}(t - t_{M-1}) \right] \tag{65}$$

Using (65) we can analytically evaluate, following [15], the single step integral term of (64) for the ith exponential function as

$$\int_{(M-1)\Delta t}^{M\Delta t} \left[A_i e^{B_i \omega_{ab}(M\Delta t - \tau)} \right] E_{p,j}(\tau) d\tau = \frac{A_i}{(B_i \omega_{ab})^2 \Delta t} \left[\begin{array}{l} E_{p,j}^{M-1} \left(B_i \omega_{ab} \Delta t e^{B_i \omega_{ab} \Delta t} - e^{B_i \omega_{ab} \Delta t} + 1 \right) \\ + E_{p,j}^{M} \left(e^{B_i \omega_{ab} \Delta t} - B_i \omega_{ab} \Delta t - 1 \right) \end{array} \right] \tag{66}$$

This convolution implementation leads to a FETD formulation that is faster than the one presented in [1] where two convolutions, one internal and one external, need to be computed.

4   Numerical Results

In this section, numerical results are presented to demonstrate the accuracy, stability and speed of the VF-RC-FETD-FABC code. Four models are considered: an infinitely thin perfectly electrically conducting (PEC)

metallic grating (2D structure with y-direction uniformity) [16], a dielectric block periodic structure [17], an annular aperture FSS [18] and a microstrip patch FSS [1]. In the simulations, a desktop PC with CPU speed 2.79GHz and 2.5Gbytes of memory was used. In all models, the non-periodic boundaries S_1 and S_2 are placed in free space and it is assumed that $z_1 = 0$.

The time variation of the incident field is

$$I_0(t) = \exp\left[-0.5\left(\frac{t-t_d}{t_w}\right)^2\right]\sin(2\pi f_c t) \tag{67}$$

where the parameter t_d denotes a time delay, t_w determines the pulse width and f_c is the central frequency. These parameters as well as the number of harmonics, the time step and the number of time steps (NTS), for each of the models, are listed in Table-2.

For the post-processing, the frequency domain tangential component of the vector amplitude of the (m,n)th reflected and transmitted harmonics at the two non-periodic boundaries is calculated as follows (refer to (13) and (14))

$$\mathbf{R}_{t,mn} = \mathrm{DFT}\left[\frac{1}{\alpha}\int_{S_1}\mathbf{E}_{p,t}(z_1,t)e^{+j\boldsymbol{\rho}_{t,mn}\bullet\mathbf{r}}dS\right]e^{-jk_{z,mn}z_1} - \delta_{mn,00}\mathrm{DFT}\left[\mathbf{I}_{t,00}(t)\right]e^{-2jk_{z,mn}z_1} \tag{68}$$

$$\mathbf{T}_{t,mn} = \mathrm{DFT}\left[\frac{1}{\alpha}\int_{S_2}\mathbf{E}_{p,t}(z_2,t)e^{+j\boldsymbol{\rho}_{t,mn}\bullet\mathbf{r}}dS\right]e^{+jk_{z,mn}z_2} \tag{69}$$

where DFT stands for the discrete Fourier transform. Using (12), the normal component of the vector amplitude of the (m,n)th scattered harmonic in (6-7) is calculated. The normalized reflected and transmitted power carried by the (m,n)th propagating Floquet harmonic is

$$P_{mn}^{ref}\Big|_{z_1} = \frac{k_{z,mn}}{k_{z,00}}\frac{\left|\mathbf{R}_{t,mn} + R_{z,mn}\hat{\mathbf{z}}\right|^2}{\left|\mathbf{I}_{t,00} + I_{z,00}\hat{\mathbf{z}}\right|^2} \tag{70}$$

$$P_{mn}^{tran}\Big|_{z_2} = \frac{k_{z,mn}}{k_{z,00}}\frac{\left|\mathbf{T}_{t,mn} + T_{z,mn}\hat{\mathbf{z}}\right|^2}{\left|\mathbf{I}_{t,00} + I_{z,00}\hat{\mathbf{z}}\right|^2} \tag{71}$$

where $k_{z,mn}$ has a non-negative real value.

The first model is an infinitely thin PEC grating which is uniform along the y-direction. This is a 2D problem. Its periodic unit cell geometry and dimensions are given in [16]. This model has low computation requirements and allows a comparison to be made between the 3D VF-RC-FETD-FABC results and those obtained from a previously validated 2D FETD code [19]. The 3D unit cell geometry is obtained by uniformly extruding the 2D

unit cell geometry along the y-direction by a distance D_y. $D_x = 0.05$m and $D_y = 0.005$m. The distance between a non-periodic boundary and the infinitely thin PEC grating is $d_a=0.25D_x$. In Fig.2, assuming $(\theta^{inc}, \phi^{inc}) = (0^o, 0^o)$, the results of two VF-RC-FETD-FABC simulations, one using a coarse mesh and the other using a refined mesh, are compared with CST 3D results [20], 3D FEFD results, Finite Difference Time Domain (FDTD) results [16] and 2D FETD results [19]. There is a good agreement between all results. The excellent agreement between the 3D VF-RC-FETD-FABC and 3D FEFD results confirms the correct functioning of the proposed recursive convolution implementation of the time-domain FABC with the aid of VF. Fig.2 shows that the accuracy of the 3D VF-RC-FETD-FABC results is improved if more finite elements are used (i.e. if a finer mesh is employed). This is also true for the 2D FETD simulations. Furthermore, for a given number of finite elements, more accurate results are obtained by using higher order elements. This is illustrated in references [21, 22].

The second structure is a dielectric slab with periodically implanted dielectric blocks [17]. The dimensions of the unit cell and the material properties are shown in Fig.3. The incident plane wave is TM polarised ($\eta^{inc}=90^o$) and the angle of incidence is $(\theta^{inc}, \phi^{inc}) = (30^o, 0^o)$. The magnitude of the co-polarised reflection coefficient of the fundamental harmonic is given by $\left|\Gamma_{00}^{TM}\right| = \left|R_{x,00}\right|/\left|I_{x,00}\right|$, refer to (13) and (1). It is plotted in Fig.4. The VF-RC-FETD-FABC results are compared with those of [17] and the CST [20]. Note that a very good agreement is observed between the VF-RC-FETD-FABC and the CST results for this all-dielectric periodic structure.

The third model is a PEC plate of finite thickness perforated with annular apertures [18]. The unit cell is shown in Fig.5. The incident wave is assumed to be TM ($\eta^{inc}=90^o$) polarised. The angle of incidence is $(\theta^{inc}, \phi^{inc}) = (25^o, 0^o)$. The non-periodic FE mesh boundaries are deliberately made to coincide with the plate faces ($d_a = 0$) in order to reduce the FE mesh size. Therefore, the Floquet absorbing boundary condition must contain a significant number of evanescent higher order harmonics. In Fig.6 the normalised total transmitted power is shown. It is obtained by summing up the normalised powers carried by all the propagating transmitted harmonics. There is a good agreement between the VF-RC-FETD-FABC results and those of [18] and the CST. The accuracy of the VF-RC-FETD-FABC results improves as the number of evanescent harmonics, taken into account in the FABC, increases. This is demonstrated in Fig.6 where it can be seen that the accuracy of the FETD results is improved by increasing the number of harmonics from $(M_F = N_F =3)$ to $(M_F = N_F =5)$. Assuming all propagating harmonics are accounted for, the number of (M_F, N_F) harmonics can be kept small provided that the non-periodic FE mesh boundaries are placed sufficient away from the periodic structure so that the evanescent field value at these

boundaries is negligible. However, this means that a larger number of finite elements must be employed. Due to computer memory constrains and the fact that the correct functioning of the 3D VF-RC-FETD-FABC code has already been demonstrated, which is the aim of our paper, an extended mesh was not employed.

The fourth structure is an FSS consisting of an array of rectangular PEC microstrip patches [1]. The patches are embedded in a dielectric slab. The dimensions of the unit cell and the material properties are shown in Fig.7. The incident plane wave is TE polarised (η^{inc}=0º) and the angle of incidence is (θ^{inc},ϕ^{inc}) = (30º, 0º). In Fig.8, the VF-RC-FETD-FABC results for the normalized reflected power carried by the (m,n) = (0,0) fundamental Floquet harmonic are compared with those of [1] and the CST. Although due to computer memory constrains, a modest number of elements was employed, there is a good agreement between all sets of results. The shift, in Fig.8 between our results and those of [1] and CST, at low frequencies, is not due to the RC but to the FE spatial discretisation accuracy, i.e. more accurate results are expected if the mesh is refined and higher order elements are employed [21, 22]. In [23] (page 392) a similar shift is obtained between two sets of results when modeling a similar structure. The first set of results was obtained using the 6 d.o.f. tedrahedral element employed in this paper and the second set of results was obtained using a higher order element.

We consider the model in Fig.7 in order to demonstrate the achieved time window of practical stability. The arrow in its unit cell mesh indicates the edge, located on surface S_1, at which the transient results are recorded. In Fig.9, the transient results of four methodologies are compared: (i) the 3D MS-RC-FETD-FABC method which employs the trapezoidal integration rule in the RC computation and it is based on [4]; (ii) the VF-RC-FETD-FABC method which employs the trapezoidal integration rule in the RC computation; (iii) the 3D MS-RC-FETD-FABC method which employs the triangular temporal basis function (65) in the RC computation; and (iv) the VF-RC-FETD-FABC method which employs the triangular temporal basis function in the RC computation. The figure shows that the latter methodology achieves a remarkably large time window of practical stability, at least 10 times larger than those of the other methodologies for this model. The reason was found to be the improved accuracy of the convolution computation through the use of the triangular functions and the VF method. In addition, a small time step leads to better accuracy in the calculation of the convolution.

The Courant limit (Table-2) provides a good initial estimation for the time step value Δt. The actual value of Δt (Table-2) was determined heuristically such that the early onset of instability is avoided. It was also heuristically found that Δt may be larger that the Courant limit value (dielectric blocks model, Table-2). Since the size of time step depends on the FE mesh, the frequency range of interest, the number of Floquet harmonics and the angle of

incidence [19], the heuristically chosen value of Δt may need to be reduced further as the order of the harmonics taken into account in the FABC or the angle of incidence increases.

The computational speed of the proposed method is demonstrated by comparing, for 5000 time steps, the simulation time of the 3D VF-RC-FETD-FABC code with that of a code using SC with trapezoidal integration. The recorded times do not include the assembly and inversion of the global finite element matrix which is done prior to the time marching process. The times are listed in Table-3. For these simulations, the 3D VF-RC-FETD-FABC is faster by a factor of at least 3.5. The 3D VF-RC-FETD-FABC simulation time for 20000 time steps is also shown indicating that there is a linear increase of computation time with the number of time steps. As expected, Table-3 shows that the simulation time increases when the mesh density and the number of Floquet harmonics increase.

5   Conclusion

It is shown that the VF-RC-FETD-FABC formulation is faster than the SC formulation. Furthermore, since the proposed VF-RC is a single section RC, it dispenses with the time taken to decide the number and the limits of the sections in the MS RC implementation in [4].

The proposed 3D VF-RC-FETD-FABC method is practically stable over a temporal window that is larger than that of the 3D MS-RC-FETD-FABC. Thus for many practical problems, as suggested in [24], a stability correction scheme is not necessary. This is particularly true when extrapolation can be employed [25]. It is expected that the combination of recursive convolution and extrapolation will result in a very fast software and it is the subject of a future paper.

For problems requiring long FETD simulation times, further research is needed to develop a suitable stability correction scheme (similar to the one employed in [24] for simple FETD problems) for our fast VF-RC-FETD-FABC code.

It must be noted that the stability analysis of the VF-RC-FETD-FABC is a difficult task because of the complexity of the VF-RC-FETD-FABC formulation and it will also be the subject of future research.

6   Appendix

From (25-26, 28-29), the frequency domain expression of $\Omega^g(\omega)$ is obtained

$$\Omega^g(\omega)\Big|_{g=1,2} = \sum_{m=-\infty}^{\infty}\sum_{n=-\infty}^{\infty}\left(\frac{\gamma_{z,mn}}{\alpha}\right)\left(\int_{S_g} \mathbf{W}_{p,t}\, e^{-j\boldsymbol{\rho}_{t,mn}\bullet\mathbf{r}}\,dS\right)\bullet\left(\int_{S_g}\mathbf{E}_{p,t}\, e^{+j\boldsymbol{\rho}_{t,mn}\bullet\mathbf{r}}\,dS\right)$$
$$+\sum_{m=-\infty}^{\infty}\sum_{n=-\infty}^{\infty}\left(\frac{-1}{\alpha\gamma_{z,mn}}\right)\left(\mathbf{k}_{t,mn}\bullet\int_{S_g}\mathbf{W}_{p,t}\,e^{-j\boldsymbol{\rho}_{t,mn}\bullet\mathbf{r}}\,dS\right)\left(\mathbf{k}_{t,mn}\bullet\int_{S_g}\mathbf{E}_{p,t}\,e^{+j\boldsymbol{\rho}_{t,mn}\bullet\mathbf{r}}\,dS\right) \tag{72}$$

Prior to obtaining the time domain expression of $\Omega^g(\omega)$, (72) is expanded and re-written as follows with $s = j\omega$.

$$\Omega^g(s)\Big|_{g=1,2} = \sum_{m=-\infty}^{\infty}\sum_{n=-\infty}^{\infty}\xi_{mn}^{(1)}(s)\left(\int_{S_g}\mathbf{W}_{p,t}\,e^{-j\boldsymbol{\rho}_{t,mn}\bullet\mathbf{r}}\,dS\right)\bullet\left(\int_{S_g}\mathbf{E}_{p,t}\,e^{+j\boldsymbol{\rho}_{t,mn}\bullet\mathbf{r}}\,dS\right)$$
$$+\sum_{m=-\infty}^{\infty}\sum_{n=-\infty}^{\infty}\xi_{mn}^{(2)}(s)\left(\int_{S_g}W_{p,x}\,e^{-j\boldsymbol{\rho}_{t,mn}\bullet\mathbf{r}}\,dS\right)\left(\int_{S_g}E_{p,x}\,e^{+j\boldsymbol{\rho}_{t,mn}\bullet\mathbf{r}}\,dS\right)$$
$$+\sum_{m=-\infty}^{\infty}\sum_{n=-\infty}^{\infty}\xi_{mn}^{(3)}(s)\left(\int_{S_g}W_{p,y}\,e^{-j\boldsymbol{\rho}_{t,mn}\bullet\mathbf{r}}\,dS\right)\left(\int_{S_g}E_{p,y}\,e^{+j\boldsymbol{\rho}_{t,mn}\bullet\mathbf{r}}\,dS\right)$$
$$+\sum_{m=-\infty}^{\infty}\sum_{n=-\infty}^{\infty}\xi_{mn}^{(4)}(s)\left[\begin{array}{c}\left(\int_{S_g}W_{p,x}\,e^{-j\boldsymbol{\rho}_{t,mn}\bullet\mathbf{r}}\,dS\right)\left(\int_{S_g}E_{p,y}\,e^{+j\boldsymbol{\rho}_{t,mn}\bullet\mathbf{r}}\,dS\right)\\[2mm]+\left(\int_{S_g}W_{p,y}\,e^{-j\boldsymbol{\rho}_{t,mn}\bullet\mathbf{r}}\,dS\right)\left(\int_{S_g}E_{p,x}\,e^{+j\boldsymbol{\rho}_{t,mn}\bullet\mathbf{r}}\,dS\right)\end{array}\right] \tag{73}$$

The four frequency dependent functions $\xi_{mn}^{(q)}(s)$ in (73) are

$$\xi_{mn}^{(1)}(s) = \frac{\cos\theta^{inc}}{c\alpha}\sqrt{\left(s-j\omega_a\right)^2+\omega_{ab}^2} \tag{74}$$

$$\xi_{mn}^{(2)}(s) = \frac{1}{c\alpha\cos\theta^{inc}}\frac{\left(\tau_x s + jc\rho_{xm}\right)^2}{\sqrt{\left(s-j\omega_a\right)^2+\omega_{ab}^2}} \tag{75}$$

$$\xi_{mn}^{(3)}(s) = \frac{1}{c\alpha\cos\theta^{inc}}\frac{\left(\tau_y s + jc\rho_{yn}\right)^2}{\sqrt{\left(s-j\omega_a\right)^2+\omega_{ab}^2}} \tag{76}$$

$$\xi_{mn}^{(4)}(s) = \frac{1}{c\alpha\cos\theta^{inc}}\frac{\left(\tau_x s + jc\rho_{xm}\right)\left(\tau_y s + jc\rho_{yn}\right)}{\sqrt{\left(s-j\omega_a\right)^2+\omega_{ab}^2}} \tag{77}$$

where

$$\omega_a = c\left(\tau_x\rho_{xm}+\tau_y\rho_{yn}\right)\big/\cos^2\theta^{inc} \tag{78}$$

$$\omega_b^2 = c^2\left(\rho_{xm}^2+\rho_{yn}^2\right)\big/\cos^2\theta^{inc} \tag{79}$$

$$\omega_{ab} = \sqrt{\omega_a^2+\omega_b^2} \tag{80}$$

Applying the ILT to (73), $\Omega^g(t)$ is obtained

$$\Omega^g\left(t\right)\Big|_{g=1,2} = \sum_{m=-\infty}^{\infty}\sum_{n=-\infty}^{\infty}\left(\int_{S_g} \mathbf{W}_{p,t}\, e^{-j\mathbf{p}_{t,mn}\bullet\mathbf{r}}\,dS\right)\bullet\xi_{mn}^{(1)}\left(t\right)*\left(\int_{S_g} \mathbf{E}_{p,t}\left(t\right)e^{+j\mathbf{p}_{t,mn}\bullet\mathbf{r}}\,dS\right)$$
$$+\sum_{m=-\infty}^{\infty}\sum_{n=-\infty}^{\infty}\left(\int_{S_g} W_{p,x}e^{-j\mathbf{p}_{t,mn}\bullet\mathbf{r}}\,dS\right)\xi_{mn}^{(2)}\left(t\right)*\left(\int_{S_g} E_{p,x}\left(t\right)e^{+j\mathbf{p}_{t,mn}\bullet\mathbf{r}}\,dS\right)$$
$$+\sum_{m=-\infty}^{\infty}\sum_{n=-\infty}^{\infty}\left(\int_{S_g} W_{p,y}e^{-j\mathbf{p}_{t,mn}\bullet\mathbf{r}}\,dS\right)\xi_{mn}^{(3)}\left(t\right)*\left(\int_{S_g} E_{p,y}\left(t\right)e^{+j\mathbf{p}_{tmn}\bullet\mathbf{r}}\,dS\right)$$
$$+\sum_{m=-\infty}^{\infty}\sum_{n=-\infty}^{\infty}\left[\begin{array}{c}\left(\int_{S_g} W_{p,x}e^{-j\mathbf{p}_{t,mn}\bullet\mathbf{r}}\,dS\right)\xi_{mn}^{(4)}\left(t\right)*\left(\int_{S_g} E_{p,y}\left(t\right)e^{+j\mathbf{p}_{tmn}\bullet\mathbf{r}}\,dS\right)\\+\left(\int_{S_g} W_{p,y}e^{-j\mathbf{p}_{t,mn}\bullet\mathbf{r}}\,dS\right)\xi_{mn}^{(4)}\left(t\right)*\left(\int_{S_g} E_{p,x}\left(t\right)e^{+j\mathbf{p}_{tmn}\bullet\mathbf{r}}\,dS\right)\end{array}\right]$$

(81)

where the symbol '*' denotes the convolution operator.

The time domain functions $\xi_{mn}^{(q)}(t)$ in (81) are now derived. Consider first $\xi_{mn}^{(1)}(t)$. Let us rewrite (74) as

$$\xi_{mn}^{(1)}(s)=\frac{\cos\theta^{inc}}{c\alpha}\left\{\left[\sqrt{\left(s-j\omega_a\right)^2+\omega_{ab}^2}-\left(s-j\omega_a\right)\right]+\left(s-j\omega_a\right)\right\}$$

(82)

Consider also the following ILT [26],

$$\mathsf{L}^{-1}\left[\left(\sqrt{s^2+a^2}-s\right)^k\right]=\frac{ka^k J_k\left(at\right)}{t}\quad\left(k=1,2,\cdots\right)$$

(83)

$$\mathsf{L}^{-1}(s)=\delta'(t)$$

(84)

$$\mathsf{L}^{-1}(1)=\delta(t)$$

(85)

where $J_k(\cdot)$ is the kth order Bessel function of the first kind. $\delta(t)$ and $\delta'(t)$ are the Dirac delta function and its

time derivative respectively. Using (83-85) we can obtain the time domain expression of (82)

$$\xi_{mn}^{(1)}(t)=\frac{\cos\theta^{inc}}{c\alpha}\left[\omega_{ab}e^{j\omega_a t}\, J_1\left(\omega_{ab}t\right)/t+\delta'(t)-j\omega_a\delta(t)\right]$$

(86)

To find $\xi_{mn}^{(2)}(t)$ we make use of the ILT

$$\mathsf{L}^{-1}\left[\frac{\left(\sqrt{s^2+a^2}-s\right)^k}{\sqrt{s^2+a^2}}\right]=a^k J_k\left(at\right)\quad\left(k=0,1,2,\cdots\right)$$

(87)

from which we can derive the following

$$\mathsf{L}^{-1}\left[\frac{1}{\sqrt{s^2+a^2}}\right]=J_0\left(at\right)$$

(88)

$$\mathsf{L}^{-1}\left[\frac{s}{\sqrt{s^2+a^2}}\right]=-aJ_1\left(at\right)+\delta(t)$$

(89)

$$L^{-1}\left[\frac{s^2}{\sqrt{s^2+a^2}}\right]=\frac{aJ_1(at)}{t}-a^2J_0(at)+\delta'(t)$$

(90)

We now expand the s-fraction term in (75) as

$$\frac{(\tau_x s+jc\rho_{xm})^2}{\sqrt{(s-j\omega_a)^2+\omega_{ab}^2}}=\tau_x^2\left\{\frac{(s-j\omega_a)^2}{\sqrt{(s-j\omega_a)^2+\omega_{ab}^2}}\right\}+[2j\tau_x(\tau_x\omega_a+c\rho_{xm})]\left\{\frac{(s-j\omega_a)}{\sqrt{(s-j\omega_a)^2+\omega_{ab}^2}}\right\}-\frac{(\tau_x\omega_a+c\rho_{xm})^2}{\sqrt{(s-j\omega_a)^2+\omega_{ab}^2}}$$

(91)

Applying the ILT and (88-90) to (91), we obtain

$$L^{-1}\left[\frac{(\tau_x s+jc\rho_{x,m})^2}{\sqrt{(s-j\omega_a)^2+\omega_{ab}^2}}\right]=\tau_x^2 e^{j\omega_a t}\left[\frac{\omega_{ab}J_1(\omega_{ab}t)}{t}-\omega_{ab}^2 J_0(\omega_{ab}t)+\delta'(t)\right]$$

$$+[2j\tau_x(\tau_x\omega_a+c\rho_{x,m})]e^{j\omega_a t}[-\omega_{ab}J_1(\omega_{ab}t)+\delta(t)]$$

$$-[(\tau_x\omega_a+c\rho_{x,m})^2][e^{j\omega_a t}J_0(\omega_{ab}t)]$$

(92)

By making use of the relation [26]

$$f(t)\delta(t)=f(0)\delta(t)$$

(93)

and the product rule the following equations can be proved

$$e^{j\omega_a t}\delta(t)=\delta(t)$$

(94)

$$e^{j\omega_a t}\delta'(t)=-j\omega_a\delta(t)+\delta'(t)$$

(95)

Thus, from (92,94,95), we obtain

$$\xi_{mn}^{(2)}(t)=\frac{\cos\theta^{inc}}{c\alpha}\left\{\begin{array}{l}[-(2\omega_a^2+\omega_b^2)\tau_x^2-2c\omega_a\rho_{x,m}\tau_x-c^2\rho_{x,m}^2]e^{j\omega_a t}J_0(\omega_{ab}t)\\+[-2\omega_a\tau_x^2-2c\rho_{x,m}\tau_x]j\omega_{ab}e^{j\omega_a t}J_1(\omega_{ab}t)\\+\tau_x^2\omega_{ab}e^{j\omega_a t}J_1(\omega_{ab}t)/t\\+\tau_x^2\delta'(t)+j(2c\rho_{x,m}\tau_x+\omega_a\tau_x^2)\delta(t)\end{array}\right\}$$

(96)

The time domain expressions for (76) and (77) can be obtained in a similar way. All time functions (74-77) can be expressed in the following general form

$$\xi_{mn}^{(q)}(t)=C_0^{(q)}\left\{\begin{array}{l}C_{1,mn}^{(q)}f_{1,mn}(t)+C_{2,mn}^{(q)}f_{2,mn}(t)+C_3^{(q)}f_{3,mn}(t)\\+C_4^{(q)}\delta'(t)+jC_{5,mn}^{(q)}\delta(t)\end{array}\right\}$$

$$=h_{mn}^{(1)}(t)+C_0^{(q)}\left\{C_4^{(q)}\delta'(t)+jC_{5,mn}^{(q)}\delta(t)\right\}$$

(97)

where the coefficients are given in Table-4 and

$$f_{1,mn}(t)=e^{j\omega_a t}J_0(\omega_{ab}t)$$

(98)

$$f_{2,mn}(t) = j\omega_{ab}e^{j\omega_a t}J_1(\omega_{ab}t) \tag{99}$$

$$f_{3,mn}(t) = \omega_{ab}e^{j\omega_a t}J_1(\omega_{ab}t)/t \tag{100}$$

7   References

[1] Petersson, L. E. R., and Jin, J. M.: 'Analysis of periodic structures via a time-domain finite-element formulation with a Floquet ABC', IEEE Trans. Antennas Propag., 2006, **54**, (3), pp. 933-944

[2] Petersson, L. E. R., and Jin, J. M.: 'Three-Dimensional Time-Domain Finite-Element Formulation for Periodic Structures', IEEE Trans. Antennas Propag., 2006, **54**, (1), pp. 12-19

[3] Semlyen, A., and Dabuleanu, A.: 'Fast and accurate switching transient calculations on transmission lines with ground return using recursive convolutions', IEEE Trans. Power App. Syst., 1975, **PAS-94**, (2), pp. 561–571

[4] Cai, Y., and Mias, C.: 'Fast Finite Element Time Domain – Floquet Absorbing Boundary Condition modelling of periodic structures using recursive convolution', IEEE Trans. Antennas Propag., 2007, **55**, (9), pp. 2550-2558

[5] Gustavsen, B., and Semlyen, A.: 'Rational Approximation of Frequency Domain Responses by Vector Fitting', IEEE Trans. on Power Delivery, 1999, **14**, (3), pp. 1052-1061

[6] Rao, S. M., and Wilton, D. R.: 'Transient scattering by conducting surfaces of arbitrary shape', IEEE Trans. Antennas Propag., 1991, **39**, (1), pp.56-61

[7] Ferrari, R. L.: 'Finite element solution of time-harmonic modal field in periodic structures', Electronics Letters, 1991, **27**, (3), pp.33-34

[8] Ferrari, R. L.: 'Spatially Periodic Structures', in Itoh, T., Pelosi, G., and Silvester, P. P. (Eds.): 'Finite Element Software for Microwave Engineering', (Wiley, 1996)

[9] Watkins, D. A.: 'Topics in Electromagnetic Theory', (John Wiley & Sons, 1958)

[10] Maloney, J. G., and Kesler, M. P.: 'Analysis of periodic structures', in Taflove, A., and Hagness, S. C. (Eds.): 'Computational electrodynamics: The finite difference time domain method', (Artech House, 2000, 2nd edn.).

[11] Jin, J. M.: 'The finite element method in electromagnetics', (Wiley-IEEE press, 2002)

[12] Newmark, N. M.: 'A method of computation for structural dynamics', J. Engineering Mechanics Division, ASCE, 1959, **85**, pp. 67-94

[13] Zienkiewicz, O. C.: 'A new look at the Newmark, HouBolt, and other time-stepping formulas: a weighted residual approach', Earthquake Engineering and Structural Dynamics, 1977, **5**, pp.413-418

[14] VECTFIT package version 1. Retrieved from www.energy.sintef.no/produkt/VECTFIT/index.asp on 02/06/2008.

[15] Kelley, D. F., and Luebbers, R. J.: 'Piecewise linear recursive convolution for dispersive media using FDTD', IEEE Trans. Antennas Propag., 1996, **44**, (6), pp.792-797

[16] Navarro, E. A., Gimeno, B., and Cruz, J. L.: 'Modelling of periodic structrues using the finite difference time domain method combined with the Floquet theorem', Electronics Letters, 1993, **29**, (5), pp. 446-447

[17] Yang, H. Y. D., Diaz, R., and Alexopoulos, N. G.: 'Reflection and transmission of waves from multilayer structures with planar-implanted periodic material blocks', Journal of the Optical Society of America B, 1997, **14**, (10), pp.2513-2521

[18] Roberts, A., and McPhedran, R. C.: 'Bandpass grids with annular apertures', IEEE Trans. Antennas Propag., 1988, **36**, (5), pp.607-611

[19] Cai, Y., and Mias, C.: 'Finite-element time-domain modelling of plane wave scattering by a periodic structure using an exact boundary condition', IET Microwaves, Antennas and Propagation, 2007, **1**, (3), pp. 609-616.

[20] CST (Computer Simulation Technology) Microwave Studio (CST MWS), frequency domain solver, Darmstadt, Germany, www.cst.com.

[21] Lou, Z., and Jin, J. M.: 'High-order finite-element analysis of periodic absorbers', Microwave and Optical Technology Letters, 2003, **37**, (3), pp. 203-207

[22] Volakis, J.L., Eibert, T.F., Filipovic, D.S., Erdemli, Y.E., and Topsakal E.: 'Hybrid finite element methods for array and FSS analysis using multiresolution elements and fast integral techniques', Electromagnetics, 2002, **22**, (4), pp. 297–313

[23] Zhu, Y., and Cangellaris, A. C.: 'Multigrid finite element methods for electromagnetic field modeling', (John Wiley & Sons, 2006)

[24] Chilton, R. A., and Lee, R.: 'The discrete origin of FETD-Newmark late time instability, and a correction scheme', Journal of Computational Physics, 2007, **224**, (2), pp. 1293–1306

[25] Adve, R. S., Sarkar, T. K., Pereira-Filho, O. M. C., and Rao, S. M.: 'Extrapolation of Time-domain responses from three-dimensional conducting objects utilizing the matrix pencil technique', IEEE Trans. Antennas Propag., 1997, **45**, (1), pp. 147-156

[26] Tuma, J. J., and Walsh, R. A.: 'Engineering Mathematics Handbook', (McGraw-Hill, 1998, 4th edn.)

Acknowledgment

LIST OF FIGURE AND TABLE CAPTIONS

Figure Captions:

Fig.1: Schematic diagram of a doubly periodic structure under oblique plane wave incidence. The unit vectors u and v are perpendicular to each other and perpendicular to the direction of plane wave propagation k_0. u is perpendicular to the plane of incidence.

Fig. 2: PEC metallic grating: normalised transmitted power of each propagating Floquet harmonic, $(\theta^{inc}, \phi^{inc}) = (0°, 0°)$. Solid line: VF-RC-FETD-FABC, refined mesh, NTS = 40000. Dotted line: VF-RC-FETD-FABC, coarse mesh, NTS = 40000. Dashed line: CST. Circles: FDTD [16]. Triangles: 3D FEFD. Dotted dashed line: 2D SC-FETD [19]. The inset is a magnified version of the rectangular region enclosed by a dashed line.

Fig.3: The unit cell of the dielectric block periodic structure. $D_x = D_y = d = 20$mm, h=2mm, a=10mm, ε_2=10ε_0, ε_1=4ε_0, d_a=6mm.

Fig.4: Dielectric block periodic structure: reflection coefficient of a TM polarised incident plane wave, $(\theta^{inc}, \phi^{inc}) = (30°, 0°)$. Solid line: VF-RC-FETD-FABC. Dashed line: CST. Circles: [17].

Fig.5: The unit cell of the annular aperture FSS. $D_x = D_y = d = 1$m, h=0.1d, a=0.45d, a/b=1.125, d_a=0.

Fig.6: Annular aperture FSS: normalised total transmitted power for a TM polarised incident plane wave, $(\theta^{inc}, \phi^{inc}) = (25°, 0°)$. Solid line: VF-RC-FETD-FABC, $M_F = N_F = 5$. Dotted line: VF-RC-FETD-FABC, $M_F = N_F = 3$. Dashed line: CST. Circles: [18].

Fig.7: The unit cell of the rectangular patch FSS and its FE mesh. ε_1=2ε_0, $D_x = D_y = d = 10$mm. a=2.5mm, b=5mm, h=2mm, d_a=8mm.

Fig.8: Microstrip Patch FSS: normalised reflected power carried by the $(m, n) = (0, 0)$ Floquet harmonic, $(\theta^{inc}, \phi^{inc}) = (30°, 0°)$. Solid line: VF-RC-FETD-FABC. Dashed line: CST. Circles: [1].

Fig.9: Microstrip Patch FSS: the transient result of a field variable at the incident port. Solid line: VF-RC using the triangular basis function. Dotted-dashed line: MS-RC using the triangular basis function. Dashed line: VF-RC using the trapezoidal integration. Dotted line: MS-RC using the trapezoidal integration.

Table Captions:

Table 1: The complex coefficients of some of the exponential terms computed using VECTFIT *

Table 2: Simulation Parameters

Table 3: Comparison of simulation times using SC and RC schemes

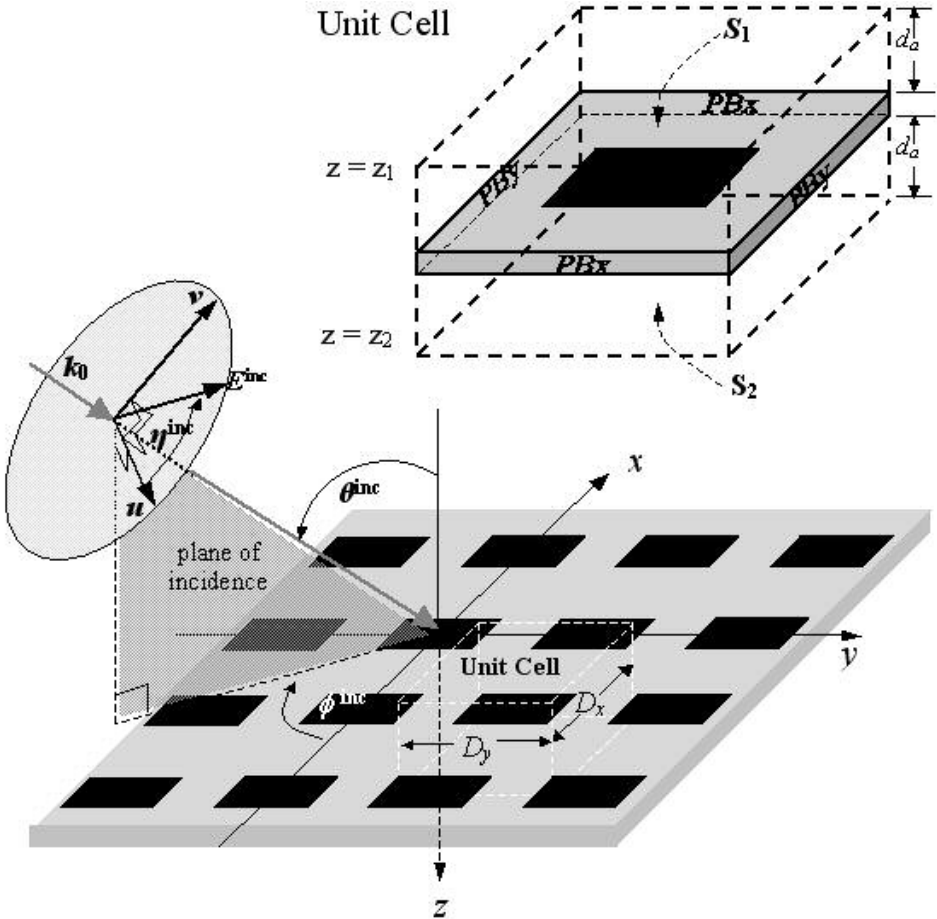**Table 4:** The coefficients of the $\xi_{mn}^{(q)}(t)$ functions
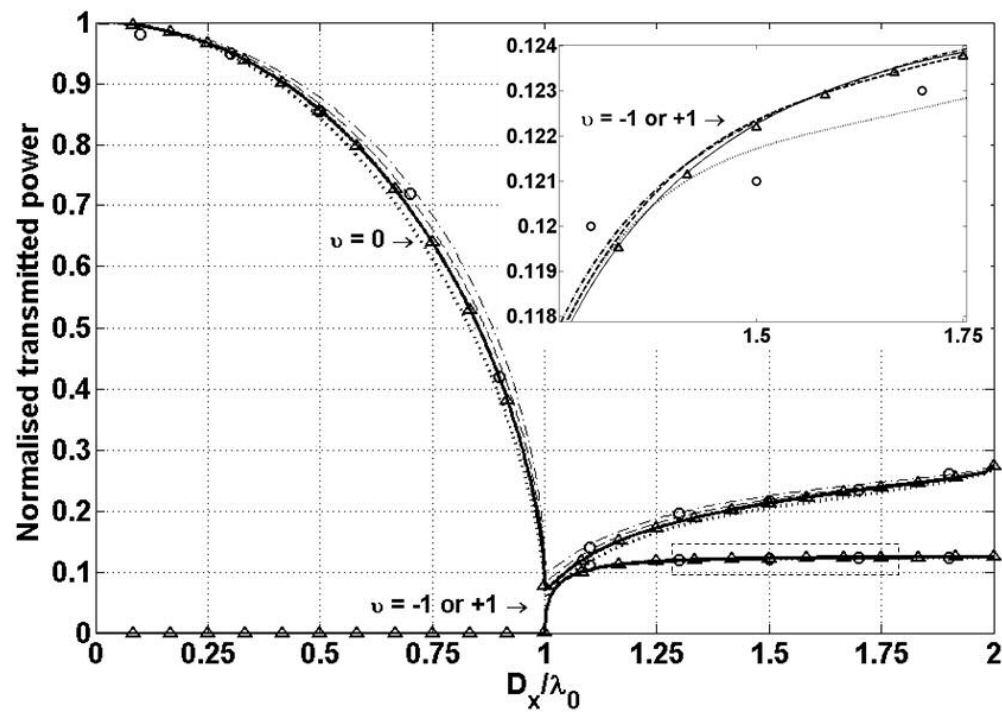
Fig.1
155x143mm (96 x 96 DPI)
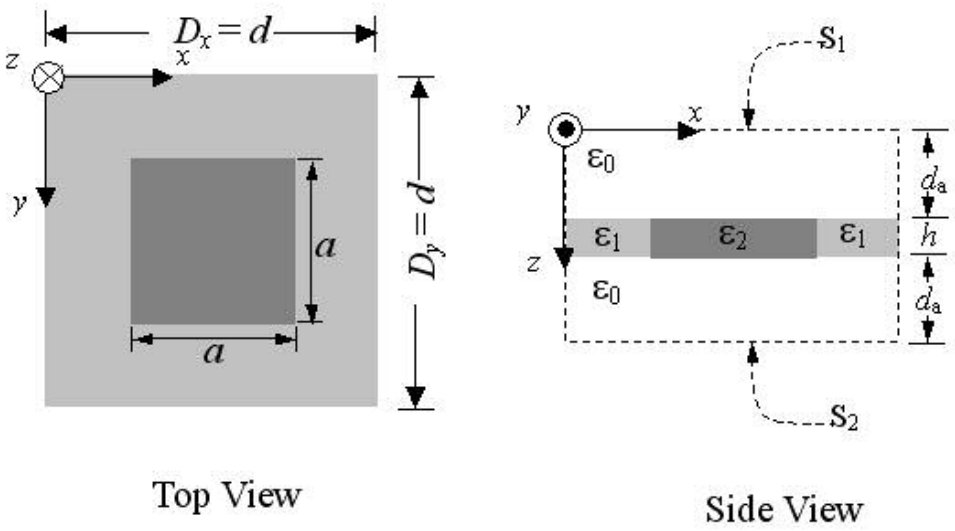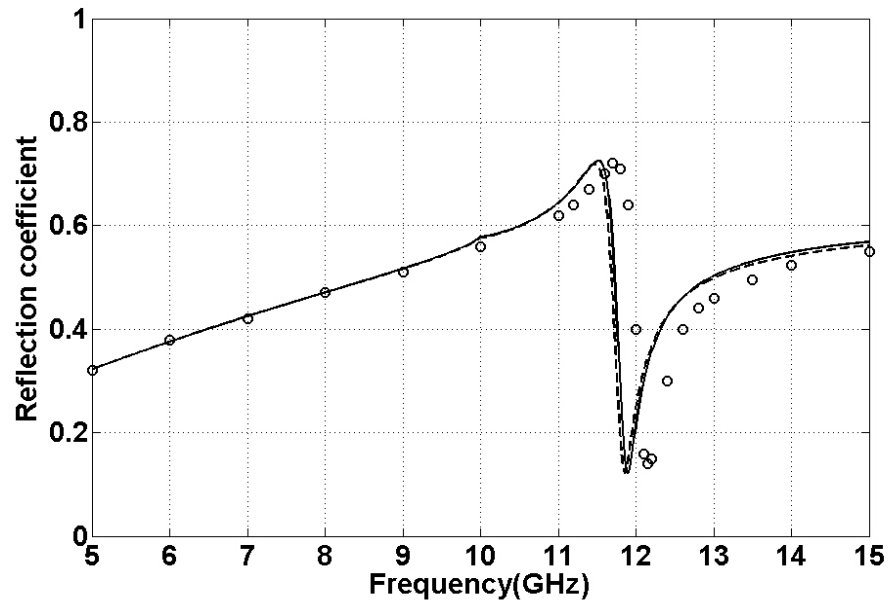
Fig.2
223x156mm (96 x 96 DPI)

Top View　　　　　　　　　　　Side View

Fig.3
144x90mm (96 x 96 DPI)

Fig.4
271x175mm (96 x 96 DPI)

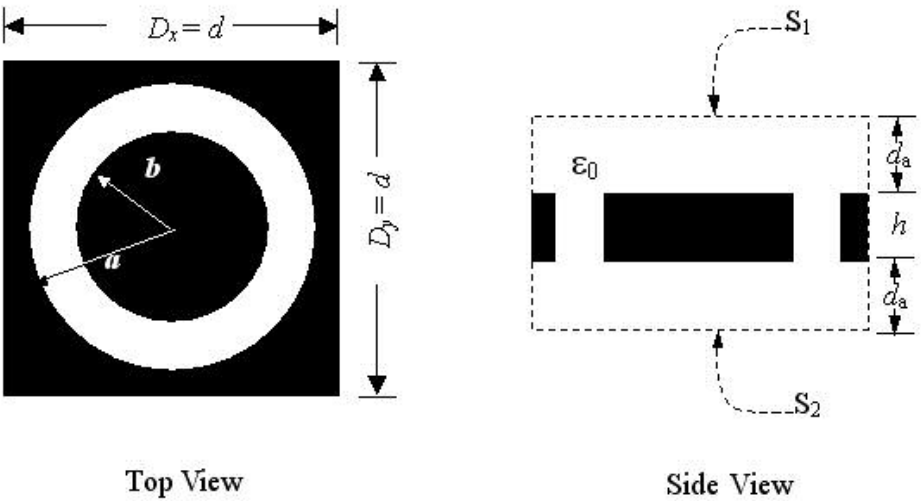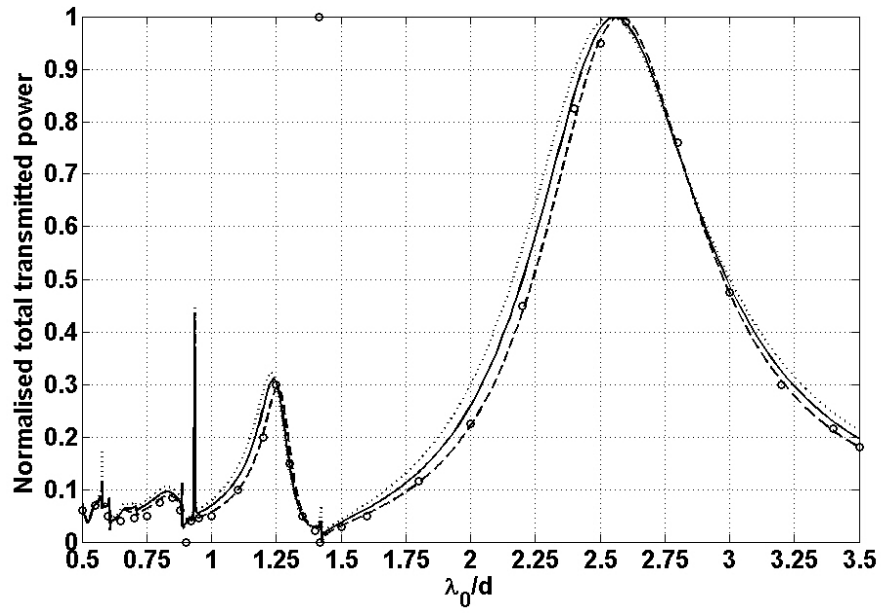Top View   Side View

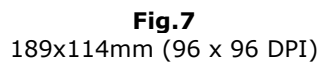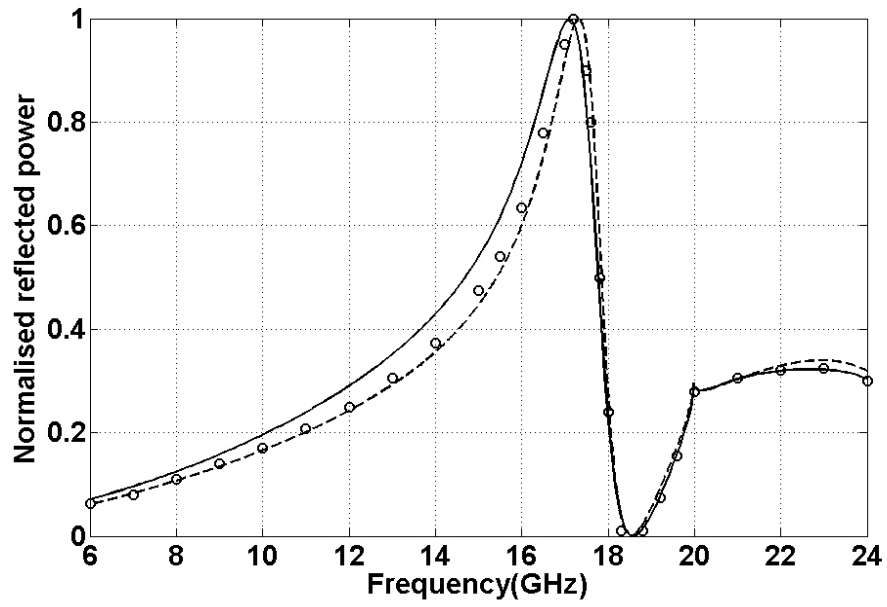**Fig.5**
153x90mm (96 x 96 DPI)

Fig.6
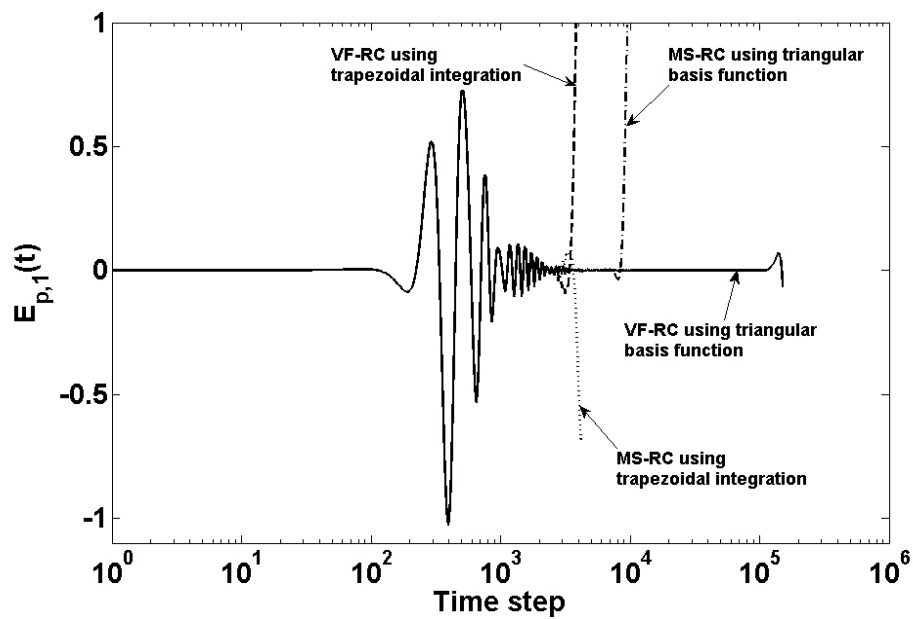271x175mm (96 x 96 DPI)

Fig.7
189x114mm (96 x 96 DPI)

Fig.8
271x175mm (96 x 96 DPI)

Fig.9
271x175mm (96 x 96 DPI)

	i	a_i
$J_0(\chi)$	1	$1.279626495406034 \times 10^{-2} - j\,1.261470741789042 \times 10^{-2}$
	…	...
	40	$1.692232579061624 \times 10^{-1} + j\,4.616465130321906 \times 10^{-2}$
	i	b_i
	1	$-1.925991503098565 \times 10^{-2} + j\,9.997590587172485 \times 10^{-1}$
	…	...
	40	$-1.140988539120197 - j\,4.335711675669561 \times 10^{-1}$
$J_1(\chi)$	i	a_i
	1	$-2.592296266238222 \times 10^{-2} - j\,3.573479902713371 \times 10^{-2}$
	…	...
	40	$1.445282983410766 \times 10^{-1} + j\,8.698222798656163 \times 10^{-2}$
	i	b_i
	1	$-1.107723835947839 \times 10^{-1} + j\,9.932592820027151 \times 10^{-1}$
	…	...
	40	$-1.003372046142869 - j\,3.612988278778275 \times 10^{-1}$
$J_1(\chi)/\chi$	i	a_i
	1	$2.114140046169769 \times 10^{-1} - j\,9.277612166889937 \times 10^{-2}$
	…	...
	24	$-1.601181589839314 \times 10^{-6} + j\,1.651034541296722 \times 10^{-6}$
	i	b_i
	1	$-8.437603910879161 \times 10^{-1} + j\,2.823005633683934 \times 10^{-1}$
	…	...
	24	$-2.349904170513284 \times 10^{-4} - j\,9.999950227350590 \times 10^{-1}$

* VECTFIT parameters: (i) number of frequency points 30000; (ii) 20 iterations.   (iii) the angular frequency range: $0 \le \omega \le 0.5\pi$ for functions $J_0(\chi)$ and $J_1(\chi)$ and $0 \le \omega \le 1.5\pi$ for $J_1(\chi)/\chi$; (iv) $Q=40$ for functions $J_0(\chi)$ and $J_1(\chi)$ and $Q=24$ for $J_1(\chi)/\chi$.

Model	θ^{inc}, ϕ^{inc}	Polarisa-tion	M_F, N_F	t_d (Δt)	t_w (Δt)	f_c (GHz)	Δt (ps)	ΔL^* (m)	Courant Limit (ps) $\dfrac{\Delta L}{c\sqrt{3}}$	NTS
Infinitely thin PEC metallic grating	0º,0º	TM	2,0	240	60	6	1.2	8.3e-4	1.6	40000
Dielectric blocks	30º,0º	TM	2,2	160	40	10	1.5	5.0e-4	0.96	50000
Annular apertures	25º,0º	TM	3,3	160	40	0.3	32	1.67e-2	32	65500
			5,5	440	110	0.3	12			95000
Microstrip Patch FSS	30º,0º	TE	2,2	400	100	15	0.3	2.1e-4	0.4	40000

* ΔL denotes the minimum edge length in the tetrahedral finite element mesh.

Model	No. of FE edges	θ^{inc}, ϕ^{inc}	M_F, N_F	Method	NTS (10^3)	Simulation Time (min)
Infinitely thin PEC metallic grating	31823 (refined mesh)	0º, 0º	2,0	RC	20	44.7
	18857 (coarse mesh)	0º, 0º	2,0	RC	20	24.9
Dielectric blocks	38693	30º, 0º	2,2	SC	5	233
				RC	5	61
					20	256
Annular apertures	5885	25º, 0º	3,3	SC	5	245
				RC	5	69
					20	276
			5,5	RC	20	701
Microstrip Patch FSS	34951	30º, 0º	2,2	SC	5	279
				RC	5	45
					20	181

$\xi_{mn}^{(1)}(t)$	$C_0^{(1)} = \cos\theta^{inc}/(c\alpha)$ $C_{1,mn}^{(1)} = C_{2,mn}^{(1)} = 0$ $C_3^{(1)} = C_4^{(1)} = 1 \qquad\qquad C_{5,mn}^{(1)} = -\omega_a$
$\xi_{mn}^{(2)}(t)$	$C_0^{(2)} = 1/(\cos\theta^{inc} c\alpha)$ $C_{1,mn}^{(2)} = -(2\omega_a^2 + \omega_b^2)\tau_x^2 - 2c\omega_a\rho_{x,m}\tau_x - c^2\rho_{x,m}^2$ $C_{2,mn}^{(2)} = -2\omega_a\tau_x^2 - 2c\rho_{x,m}\tau_x$ $C_3^{(2)} = C_4^{(2)} = \tau_x^2$ $C_{5,mn}^{(2)} = 2c\rho_{x,m}\tau_x + \omega_a\tau_x^2$
$\xi_{mn}^{(3)}(t)$	$C_0^{(3)} = 1/(\cos\theta^{inc} c\alpha)$ $C_{1,mn}^{(3)} = -(2\omega_a^2 + \omega_b^2)\tau_y^2 - 2c\omega_a\rho_{y,n}\tau_y - c^2\rho_{y,n}^2$ $C_{2,mn}^{(3)} = -2\omega_a\tau_y^2 - 2c\rho_{y,n}\tau_y$ $C_3^{(3)} = C_4^{(3)} = \tau_y^2$ $C_{5,mn}^{(3)} = 2c\rho_{y,n}\tau_y + \omega_a\tau_y^2$
$\xi_{mn}^{(4)}(t)$	$C_0^{(4)} = 1/(\cos\theta^{inc} c\alpha)$ $C_{1,mn}^{(4)} = -(2\omega_a^2 + \omega_b^2)\tau_x\tau_y - c\omega_a(\rho_{x,m}\tau_y + \rho_{y,n}\tau_x) - c^2\rho_{x,m}\rho_{y,n}$ $C_{2,mn}^{(4)} = -2\omega_a\tau_x\tau_y - c(\rho_{x,m}\tau_y + \rho_{y,n}\tau_x)$ $C_3^{(4)} = C_4^{(4)} = \tau_x\tau_y$ $C_{5,mn}^{(4)} = c(\rho_{x,m}\tau_y + \rho_{y,n}\tau_x) + \omega_a\tau_x\tau_y$